

# Ferroelectrically Gated Atomically Thin Transition-Metal Dichalcogenides as Nonvolatile Memory

Changhyun Ko, Yeonbae Lee, Yabin Chen, Joonki Suh, Deyi Fu, Aslihan Suslu, Sangwook Lee, James David Clarkson, Hwan Sung Choe, Sefaatin Tongay, Ramamoorthy Ramesh, and Junqiao Wu\*

Synergy between materials of dissimilar dimensionalities and functionalities may lead to new properties and device applications. By virtue of extremely high area-to-volume ratio and susceptibility to external stimulus, atomically thin, nearly 2D materials are suitable for constituting planar heterostructures by coupling with other 2D counterparts<sup>[1–5]</sup> or different dimensional structures including 1D nanowires<sup>[6]</sup> and 3D, thick films.<sup>[7]</sup> The recent boost of interest in semiconducting layered transition-metal dichalcogenides (TMDs) originates from their exotic characteristics in the monolayer limit, such as indirect-to-direct band gap transition,<sup>[8]</sup> valley-dependent polarization,<sup>[9]</sup> tightly bound excitonic states,<sup>[10]</sup> and piezoelectricity.<sup>[11]</sup> Besides fundamental studies, various applications have also been demonstrated, ranging from conventional field-effect transistors (FETs) to more advanced structures for potentially overcoming the scaling limit of current complementary metal-oxide-semiconductor (CMOS) technology or achieving mechanically flexible devices.<sup>[1,12–16]</sup> However, there are still a variety of functionalities found in other, bulk functional materials but not in 2D TMDs.

Ferroelectric (FE) materials, in which spontaneous polarization exists and can be reversed with the application of electric fields, are of great interest for a wide range of applications, such as ferroelectric random access memory (FeRAM),<sup>[17–19]</sup>

actuators,<sup>[20]</sup> sensors,<sup>[21]</sup> and microwave circuits.<sup>[22]</sup> It is, therefore, desirable that these properties missing in TMDs be complemented by interfacing the 2D TMDs with such functional materials, forming a synergistic system to offer new functionalities that neither of the two components alone can do. For example, the ferroelectric field-effect transistor (FeFET), in which the gate dielectric in a conventional FET is replaced with a FE film, has been considered as a potential candidate for future memory.<sup>[17,18,23–25]</sup> The advantage of this FET-type FeRAM cells is that their readout operation is nondestructive, unlike the capacitor-type FeRAMs that are destructive reads and thus need to be re-written after every readout process. However, memory stability and integration density of FeFETs need to be much improved to become a competitive memory technology. The memory instability is caused by depolarization field weakening the FE polarization, as well as interdiffusion of ions and chemical reaction across the semiconductor/FE interface that occurs when the FE film undergoes high-temperature annealing. To circumvent the chemical instability issue, dielectric buffer layers such as SiO<sub>2</sub> and HfO<sub>2</sub> are generally inserted into the interface, but they bring about additional issues such as deterioration of electrical breakdown strength and memory retention.

In addition to expected benefits in terms of size scaling, the 2D/FeFET structure where a 2D TMD layer is employed as a semiconductor channel in FeFETs have two major advantages over existing thin-film FeFET memories that use conventional semiconductor channels. First, the van der Waals (vdW) interface in the TMD/FE heterostructures largely eliminates the interfacial issues. Secondly, the ultra-thin thickness of the 2D TMD channel would facilitate accumulation of compensating charges to screen the polarization in the FE, effectively suppressing the depolarization field.<sup>[26,27]</sup> Previously, 2D/FeFETs have been demonstrated based on 2D MoS<sub>2</sub> as well as black phosphorus coated with organic FE films, respectively, and further CMOS memory circuits have been also constructed combining the two elements by Lee et al.<sup>[28,29]</sup> Using the similar structures of few-layer MoS<sub>2</sub>/organic FE, high performance photodetectors have been lately developed by Wang et al.<sup>[30]</sup> However, the applicability of organic FeFET is hampered by slow dipole dynamics, high operation voltage, and low mechanical and thermal durability in comparison to its inorganic counterparts.<sup>[28,29,31]</sup> Recently, a couple of groups have investigated inorganic FeFETs interfacing 2D MoS<sub>2</sub> n-type channels with Pb[Zr<sub>x</sub>Ti<sub>1-x</sub>]O<sub>3</sub> films, but the device performance still falls short of those of thin-film-based FeFETs, especially in terms of switching speed, and the underlying mechanisms of memory operation across 2D/FE interfaces were poorly understood.<sup>[32,33]</sup>

Dr. C. Ko, Dr. Y. Lee, Dr. Y. Chen, Dr. J. Suh, Dr. D. Fu,<sup>[†]</sup>  
Prof. S. Lee,<sup>[††]</sup> J. D. Clarkson, Dr. H. S. Choe,  
Prof. R. Ramesh, Prof. J. Wu  
Department of Materials Science and Engineering  
University of California  
Berkeley, Berkeley, CA 94720, USA  
E-mail: wuj@berkeley.edu



Dr. A. Suslu, Prof. S. Tongay  
School for Engineering of Matter  
Transport and Energy  
Arizona State University  
Tempe, AZ 85287, USA

Prof. R. Ramesh  
Department of Physics  
University of California  
Berkeley, Berkeley, CA 94720, USA

Prof. R. Ramesh, Prof. J. Wu  
Materials Sciences Division  
Lawrence Berkeley National Laboratory  
Berkeley, CA 94720, USA

<sup>[†]</sup>Present address: Department of Chemistry, National University  
of Singapore, 3 Science Drive 3 Singapore 117543, Singapore

<sup>[††]</sup>Present address: School of Materials Science and Engineering, Kyungpook  
National University, 80 Daehakro, Bukgu, Daegu 41566, Republic of Korea

DOI: 10.1002/adma.201504779

Additionally, it is noteworthy that only MoS<sub>2</sub> has been used for the 2D TMD memories, despite the existence of a large variety of members in the TMD family.<sup>[1,15,16,28,30,32–34]</sup>

In this work, we demonstrate nonvolatile memory (NVM) devices adopting mono- to few-layer TMDs (WSe<sub>2</sub> for p-type and MoS<sub>2</sub> for n-type) as the channels and epitaxial PZT (Pb[Zr<sub>0.2</sub>Ti<sub>0.8</sub>]O<sub>3</sub>) thin films as the FE layers. Using pulsed voltage waves with duration and ramping time scales down to 1 ms and 10 μs, respectively, much faster memory switching has been achieved in our solid-state 2D memories in comparison to previous 2D FeFETs that are mostly operated with organic FE. In addition, employing monolayer/FeFET structures, a nonvolatile optical memory effect has been realized, in which the photoluminescence (PL) intensity can be controlled reversibly via the FE gating, closely pertaining to understanding the mechanisms of FE effect on 2D TMDs. Moreover, the excellent stability of optical memory under long-term FE gating indicates that the limit of memory retention of FeFETs imposed by depolarization fields can be overcome by adopting 2D channels.

Considering recent developments in TMD growth, such as that by Nguyen et al. demonstrating CVD growth of monolayer MoS<sub>2</sub> on LiNbO<sub>3</sub> FE single crystals, our approach may open a pathway to 2D/FeFET memory devices with superior performance and scalable fabrication.<sup>[35,36]</sup>

Highly crystalline PZT thin films were prepared by pulsed laser deposition (PLD) on (001) SrTiO<sub>3</sub> (STO) substrates. A conductive SrRuO<sub>3</sub> (SRO) layer was deposited on the STO substrate prior to the PZT deposition (see Experimental Section). The quality of the PZT films was verified by X-ray diffraction (XRD), polarization versus electric field (*P*–*E*) characterization, and piezo force microscopy (PFM) (Figure S1, Supporting Information). The *P*–*E* loops show that the PZT films used in this work undergo sharp FE switching during the poling process, with a remnant polarization of ≈60 μC cm<sup>-2</sup> (Figure S1b, Supporting Information). By mechanical exfoliation and wet transfer method, mono- to few-layer crystalline TMD sheets were affixed firmly to the PZT surface, forming a vdW interface that plays the key role in the 2D/FeFET memory. Figure 1a shows

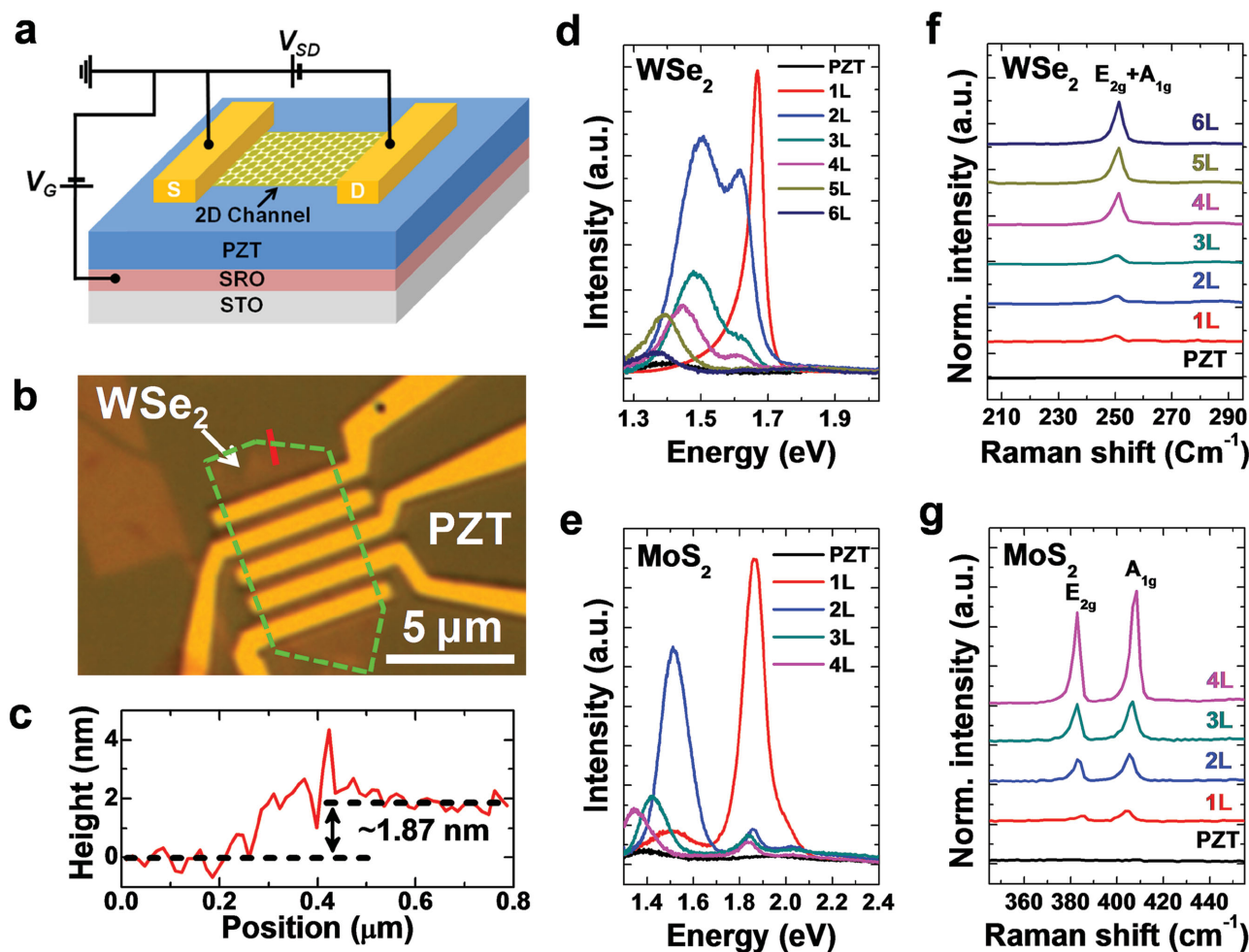


**Figure 1.** Device geometry and Raman and photoluminescence spectra. a) Device schematic of the 2D TMD/PZT heterostructure with a circuit diagram for the back-gating experiment. b) Optical image of a typical device fabricated with a 3L-WSe<sub>2</sub> channel layer and metal electrodes on PZT. c) Height profile given by contact-mode AFM along the red line in (b), validating the layer number of the WSe<sub>2</sub> channel. d and e) are PL spectra of WSe<sub>2</sub> and MoS<sub>2</sub> transferred onto PZT with various number of layers. Note that the PL intensity of 1L-WSe<sub>2</sub> in (d) is divided by 35. f,g) Raman spectra of the same sets of WSe<sub>2</sub>/PZT and MoS<sub>2</sub>/PZT samples measured in (d) and (e).

schematically device geometry of the 2D/PZT/SRO/STO along with an electric circuit for back-gating measurements. The metal lines and the conductive SRO layer were used as the top source/drain electrodes and the bottom gate terminal, respectively.

An optical microscopy image of a representative device is displayed in Figure 1b. As in the case of the three-layer (3L)-WSe<sub>2</sub> channel shown in Figure 1c, the thickness of the 2D layers was confirmed by scanning with contact-mode atomic force microscopy (AFM). Figure 1d–g summarize sets of PL and Raman spectra measured from WSe<sub>2</sub> and MoS<sub>2</sub> flakes of various thicknesses from mono- to few layers on the PZT films that were used in this study. The thickness-dependent PL and Raman characteristics are consistent with those measured from TMD layers on SiO<sub>2</sub> surface, implying that they are not structurally strained or significantly damaged during the fabrication process.<sup>[37–39]</sup>

Both p- and n-channel FeFETs were constructed using mono- or few-layer WSe<sub>2</sub> and MoS<sub>2</sub> as the p- and n-type channels, respectively, as illustrated in Figure 1a. All electrical measurements were conducted under ambient conditions. Figure 2a,b shows hysteresis loops of drain current versus gate voltage ( $I_D$ - $V_G$ ) measured from typical FeFETs based on 3L-channels. The on-off ratio was measured to be  $\approx 10^4$  at zero  $V_G$  and in the case of WSe<sub>2</sub>-based FeFET, can be enhanced up to  $\approx 10^5$  by applying a positive  $V_G$  during the reading process, comparable to state-of-art FeFET devices.<sup>[18,19]</sup> The coercive voltages ( $V_C$ ) of  $\approx \pm 2.5$  V (coercive electric fields  $\approx \pm 5$  MV m<sup>-1</sup>) are consistent

with those of the  $P$ - $E$  loop (Figure S1b, Supporting Information). The fact that the coercive field becomes smaller at lower frequency and much lower than previously reported 2D/FeFET devices (8–20 V) may be due to high dielectric constant ( $\approx 200$ ) and epitaxial quality of PZT films used in this study.<sup>[29,30,33,40–43]</sup> A slight shift of the  $I_D$ - $V_G$  curves to the negative  $V_G$  with respect to  $P$ - $E$  loops was observed due to the influence of source-drain voltage ( $V_{SD}$ ). It is a well-known feature of FE switching that the direction of the hysteresis loops is opposite to those of general FET hysteresis curves.<sup>[17,18,33]</sup> As a comparison, depletion-type FET curves acquired from both p-type and n-type 3L-TMD/PZT, in which  $V_G$  varies below  $V_C$  were also included in Figure 2a,b. It is notable that due to the high dielectric constant of PZT, the FeFET devices, even when operated in the regular FET mode, can be turned on at much lower  $V_G$  than those FETs using SiO<sub>2</sub> or high- $k$  dielectrics as the gate oxide; this low threshold  $V_G$  is advantageous for reducing power consumption of electronics.<sup>[12,14,44]</sup> The noise of  $I_D$  during the poling process is likely due to the multi-step polarization originating from the structural and chemical inhomogeneities of the PZT film, and can be suppressed by improving the quality of PZT and reducing the film thickness to facilitate concurrent poling.

The simple model for the FeFET operation illustrated in Figure 2c explains how the channel current can be modulated by the FE gating. Consider p-channel first, where positively charged holes are the majority transport carriers. When a

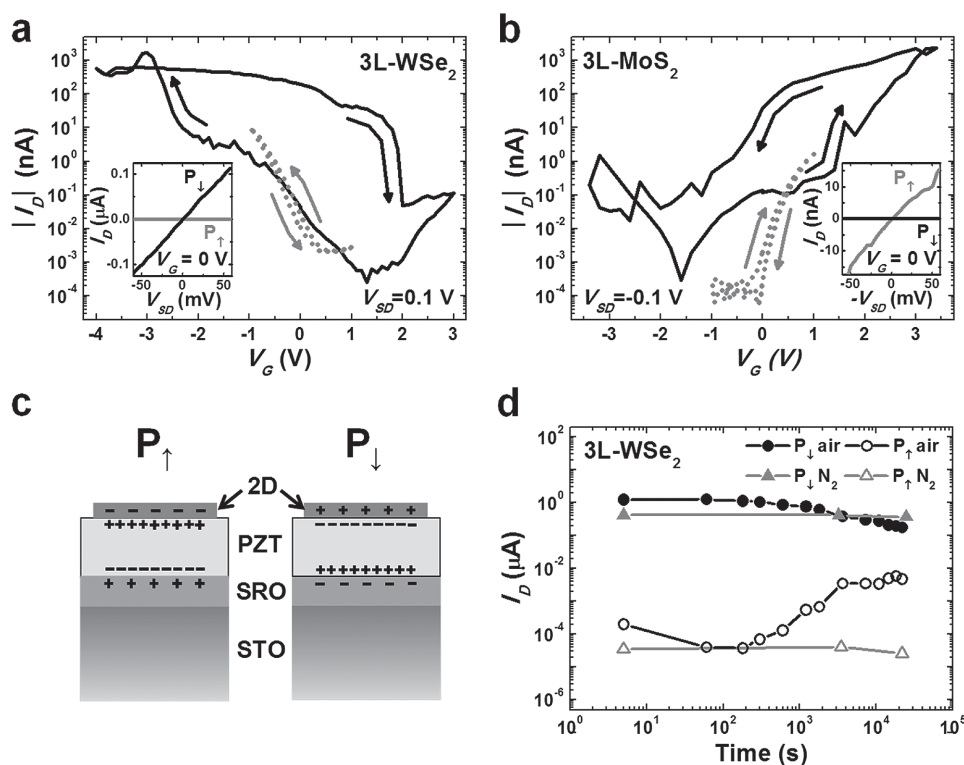


**Figure 2.** Ferroelectric field-effect transistor characteristics and memory retention. Hysteresis loops of  $I_D$ - $V_G$ , measured from representative FeFET devices based on a) p-type 3L-WSe<sub>2</sub> and b) n-type 3L-MoS<sub>2</sub> channels. Regular FET behavior of each device is also shown by limiting the  $V_G$  below the FE poling fields (dashed lines). The insets are  $I_D$ - $V_{SD}$ , curves obtained in up-polarized ( $P_{\uparrow}$ ) and down-polarized ( $P_{\downarrow}$ ) states at  $V_G = 0$  V. c) Schematic diagrams of FE gating operation in the FeFET device. d) Retention test performed on two different devices of 3L-WSe<sub>2</sub>, one stored and measured at  $V_{SD} = 0.1$  V in the ambient, and the other kept in dry N<sub>2</sub> between measurements and measured at  $V_{SD} = 0.1$  V in air.

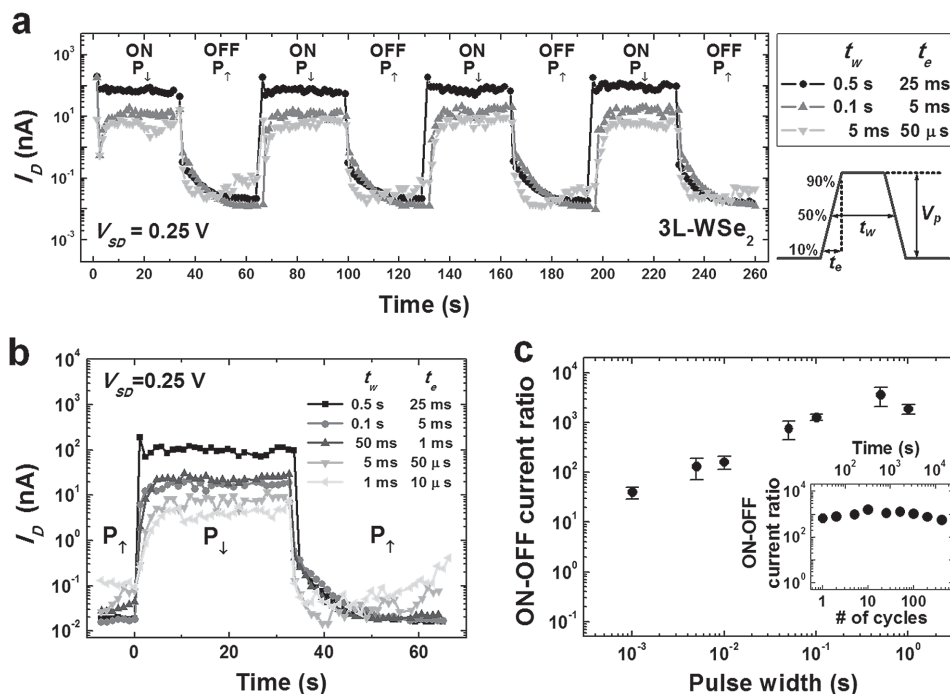


**Figure 3.** Switching operation of a ferroelectric field-effect transistor device. a) On a FeFET device based on a 3L-WSe<sub>2</sub> channel, three representative  $I_D$  versus time curves of on and off states were measured between the successive FE polings with different sets of voltage pulse parameters: peak voltage ( $V_p$ ), width ( $t_w$ ), and edge ( $t_e$ ) as defined in the inset diagram. b) A series of relaxation curves obtained from the 3L-WSe<sub>2</sub> device immediately after pulsed gating at on (down-polarized,  $P_\downarrow$ ) states and following off (up-polarized,  $P_\uparrow$ ) states at various  $t_w$  and  $t_e$  in the ranges of 0.5 s–1 ms and 25 ms–10  $\mu$ s, respectively. c) Average on–off current ratios of more than five cycles as a function of  $t_w$  with error bars of standard deviation. On–off ratio of each cycle is calculated from averaging current over 5 s after 5 s post-switching relaxation. The inset shows the data reliability test by monitoring on–off current ratio under repeated switching cycles with the pulse of 0.5 s width. Note that for all characterizations on the 3L-WSe<sub>2</sub> FeFET with the pulsed waves,  $V_{SD}$  and the read time between pulse voltage applications were fixed at 0.25 V and 30 s.  $V_p$  was set as  $-4.0$  V (on state) and  $+3.0$  V (off state) only for the voltage pulse whose  $t_w$  is 1 or 0.5 s, while  $-5.0$  V (on state) and  $+4.0$  V (off state) for the other pulses.

positive  $V_C$  is applied to the SRO bottom gate exceeding  $V_C$ , the electric dipoles in the PZT film are up-polarized ( $P_\uparrow$ ) toward the channel layer and hence, the top surface of the FE layer is positively charged. Consequently, the 2D channel is negatively charged and depleted of holes, resulting in an increase in the channel resistance. On the contrary, when the FE film is down-polarized ( $P_\downarrow$ ) by applying a bias more negative than  $-V_C$ , the hole density of 2D channel is accumulated, leading to an increase in the channel conduction. In the case of n-type channel with free electrons as the majority carriers, the channel resistance is modulated in the opposite way. Also, as shown in the insets of Figure 2a,b, the  $I_D$ – $V_{SD}$  plots were recorded in the two polarization states at zero  $V_C$ , verifying the FE-gating modulation of the channel conduction. More than 20 devices of different channel thicknesses in the range of 2L to 6L were fabricated and tested, as summarized in Figure S2 in the Supporting Information. Furthermore, the field-effect mobilities of the representative 3L-TMD channels on PZT were also analyzed and found to vary by 2–3 orders in magnitude by the FE gate. The carrier mobility of 3L-WSe<sub>2</sub> was estimated to be  $\approx 5.67$  and  $\approx 0.04$   $\text{cm}^2 \text{V}^{-1} \text{s}^{-1}$  in the  $P_\downarrow$  and  $P_\uparrow$  states, respectively. On the contrary, in 3L-MoS<sub>2</sub>, the carrier mobility is lower in the state  $P_\downarrow$  ( $\approx 0.03$   $\text{cm}^2 \text{V}^{-1} \text{s}^{-1}$ ) than the  $P_\uparrow$  state ( $\approx 23.3$   $\text{cm}^2 \text{V}^{-1} \text{s}^{-1}$ ). It is clear that both the density and mobility of majority carriers play an essential role in controlling the channel conduction with FE gating.

Memory retention tests were also carried out on the 3L-WSe<sub>2</sub> device in Figure 2d. The ratio of channel current in the on-state ( $P_\downarrow$ ) to OFF-state ( $P_\uparrow$ ) at zero  $V_C$  is initially  $\approx 10^4$ ; in ambient air, it undergoes a reduction in the first  $\approx 1.5$  h, but stabilizes at  $\approx 10^2$  for at least  $2 \times 10^4$  s, as can be seen in Figure 2d. Another 3L-WSe<sub>2</sub> device of a similar on–off ratio was stored in dry N<sub>2</sub> between measurements, and shows a much improved memory stability maintaining almost the initial on–off ratio over  $2 \times 10^4$  s, superior to those of previous 2D/FeFETs, considering that the on–off ratio can be further enhanced under a proper reading  $V_C$  lower than  $V_C$ .<sup>[28,29,32,33]</sup> The environmental effect implies that rather than self-depolarization of FE films which is the main factor causing data loss in conventional thin-film FeFETs, the main reason for the memory instability arises probably from interaction of the 2D channel with the ambient, most likely water molecules.<sup>[45]</sup> Therefore, it is expected that the memory retention can be further improved by passivating the 2D material surface with chemically inert layers, such as few-layer boron nitride.<sup>[5]</sup> To test this hypothesis, Figure 4h shows the PL intensity of a monolayer MoS<sub>2</sub> channel in the  $P_\downarrow$  and  $P_\uparrow$  states, where the PL intensity ratio lasts without much decay for over 10 d. This is an evidence of the memory retention time exceeding  $\approx 10$  d, as will be discussed in a later section.

To investigate the switching and relaxation dynamics,  $I_D$  was measured in the 2D FeFETs under periodic poling waves with pulsed voltages. Figure 3a presents three representative  $I_D$ –time

plots recorded from a p-type 3L-WSe<sub>2</sub> channel with three sets of pulse parameters of pulse voltage ( $V_p$ ), width ( $t_w$ ), and edge ( $t_e$ ). Similar successive poling measurements based on slow switching with triangular voltage waves were also performed on both p-type and n-type channels of various thickness from 2L to 6L (Figure S3, Supporting Information). The on and off currents were observed to follow the trend of the quasi-static FeFET operation (Figure 2a,b). To examine the dependence of current relaxation on  $t_w$ , the 3L-WSe<sub>2</sub> device was characterized during the read time of 30 s at both on- and off-states after applying pulsed voltages of variable  $t_w$  (0.5 s–1 ms) and  $t_e$  (25 ms–10  $\mu$ s), as summarized in Figure 3b. The initial relaxation of  $I_D$  versus time becomes clearer as  $t_w$  decreases in the both states (Figure 3b and Figure S3e, Supporting Information). The charging and discharging relaxation is likely due to the non-negligible contact resistance of the 2D channel/metal interface that causes the RC delay in conjunction with the capacitance of the PZT film. Therefore, the switching performance may be further improved by optimizing device fabrication and contacts annealing. As displayed in Figure 3c, the on-off ratio is observed to decrease monotonically with increasing switching speed, particularly when  $t_w$  is shorter than 0.5 s; this implies that there exists a delay in the response of domain wall to external fields, possibly caused by structural inhomogeneities and defects in PZT films.<sup>[43,46]</sup> However, it should be noted that the on-off current ratio stays higher than two orders of magnitude even under high speed switching with pulses whose  $t_w$  and  $t_e$  are as short as 5 ms and 50  $\mu$ s, respectively. Such a time scale of memory switching demonstrated here is much faster than previous 2D/FeFETs, including state-of-the-art 2D/organic FE memories where the poling time is in the order of

1 s. This result implies that inorganic FE would be more suitable for high-speed memory applications.<sup>[28,29]</sup>

As a further reliability test, the data endurance was also monitored under successive FE poling cycles by pulsed voltages with  $t_w$  and  $t_e$  set as 0.5 s and 50 ms, respectively. The 3L-WSe<sub>2</sub> channel shows good sustainability under over 400 cycles switching operation as shown in the inset of Figure 3c. The stability of thicker channels of 4L to 6L were also tested and summarized in Figure S3f in the Supporting Information.

Some layered TMDs, including MoS<sub>2</sub> and WSe<sub>2</sub>, have direct band gaps in the monolayer limit that offer high quantum yield of radiative exciton recombination, leading to efficient PL emission.<sup>[8,38]</sup> More interestingly, the PL characteristics, such as intensity and peak position, are strongly influenced by the bound states of electrons and holes.<sup>[37]</sup> The photoexcited electrons and holes can form either excitons (e-h pairs) or trions (e-e-h or e-h-h) even at room temperature, and accordingly, can be switched between exciton and trion emissions by controlling the free carrier type and density via external stimuli, such as electrostatic gating, physical adsorption, chemical doping, etc.<sup>[37,47,48]</sup> In addition to the electrical NVM, it is naturally expected that the PL of the channels can be also ferroelectrically modulated if monolayers are used as the 2D channels.

Figure 4a,b is optical and AFM images taken from a MoS<sub>2</sub> monolayer flake that is connected with a metal contact for back-gating through the PZT layer. The PL intensity (spectrally integrated) mapping taken on the monolayer flake after FE poling toward the two opposite states is depicted in Figure 4c,d. It is clearly seen that the PL intensity is altered significantly from the bright, P<sub>↓</sub> state, to the dark, P<sub>↑</sub> state; this occurs near the metal electrode, implying that the PZT switching is not limited

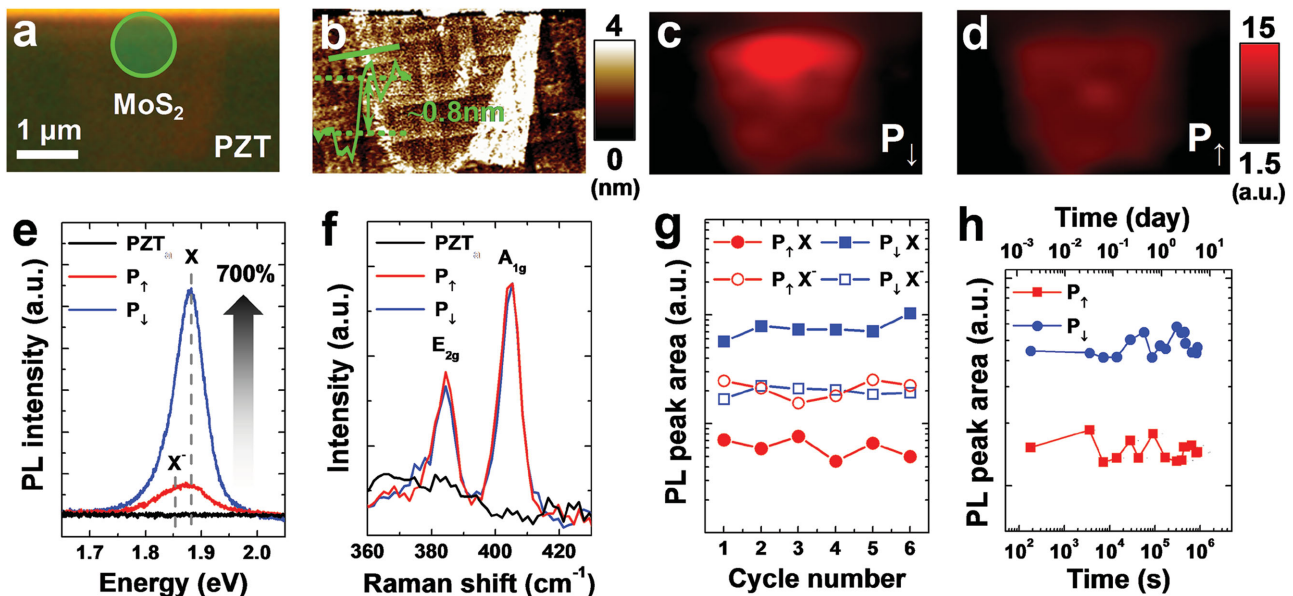


**Figure 4.** Nonvolatile photoluminescence modulation of MoS<sub>2</sub> monolayer by ferroelectric switching. a) Optical microscopy image and b) topographical map with contact-mode AFM taken from the same MoS<sub>2</sub> monolayer flake on PZT. Also, the inset of (b) shows the AFM height profile scanned from the green line, verifying the thickness of monolayer. c and d) are the maps of integrated PL intensity under down- (P<sub>↓</sub>) and up-polarized (P<sub>↑</sub>) states, respectively. e, f) PL (e) and Raman (f) spectra measured from the MoS<sub>2</sub> monolayer at both polarization states from the circle indicated in (a). PL and Raman spectra recorded from the bare PZT surface are also exhibited as a background reference. g) Variation of integrated PL intensities under multiple FE poling cycles, attributed to exciton and trion transitions obtained from fitting the PL spectra with two Lorentzian peaks. h) The stability of the ferroelectrically tuned PL was tested over 10 d using a 1L-MoS<sub>2</sub> FeFET stored in dry N<sub>2</sub> between PL acquisitions performed in ambient condition.

to directly under the top metal electrode, but also spreads out laterally by a distance up to  $\approx 1 \mu\text{m}$  from the electrode. More importantly, it is found that such lateral spreading of PZT polarization occurs only beneath the 2D TMD layer, not on the exposed PZT layer, as shown in Figure S4 in the Supporting Information where the switched FE domain is imaged with PFM. These results show that the spreading of PZT polarization is not directly by the fringing field from the top electrode, but by the 2D TMD layer that functions as a conductive pad to enhance the fringing field to pole the PZT layer underneath and therefore, for an effective operation of FE gating, the channel length should be within the scale of spreading.

As shown in Figure 4e, PL spectra were taken from the same spot (circle in Figure 4a) of the monolayer in the two polarization states, and the PL peak height was enhanced by  $\approx 700\%$  when switching from the  $P_{\uparrow}$  state to the  $P_{\downarrow}$  state. This is consistent with the fact that the emission switches from negative trion recombination to exciton recombination as the initially n-type  $\text{MoS}_2$  is depleted with electrons under the  $P_{\downarrow}$  state. As seen in Figure 4f, the Raman spectra show no significant difference between the two states. Considering that the phonon vibration modes of 1L- $\text{MoS}_2$  is quite sensitive to the external stress, the nearly identical Raman is consistent with the absence of stress difference, as the tetragonal PZT film is symmetrically polarized along  $c$ -axis in the two states, and would apply the same type and degree of stress, if any, to the  $\text{MoS}_2$  monolayer. A series of PL spectra were measured at the same spot on the flake under multiple consecutive FE switching cycles, and confirm that such nonvolatile PL modulation is reversible (Figure 4g). By fitting to the PL spectra with two Lorentzian peaks, the contributions of excitons and trions can be de-convoluted with PL peak positions at  $\approx 1.89$  and  $\approx 1.86$  eV, respectively. The exciton emission is shown to be sensitive to the external gating while the trion emission is not, in agreement with previous reports on PL behavior of 1L- $\text{MoS}_2$  under electrostatic gating.<sup>[38]</sup> As summarized in Figure S5 in the Supporting Information, the ferroelectrically tuned optical

emission was also observed on the p-type counterpart, 1L- $\text{WSe}_2$  FeFETs.

The stability of ferroelectrically modulated optical memory effect was probed using another 1L- $\text{MoS}_2$  device by tracking the integrated PL intensity of the same region in both polarization states. The device was stored in dry  $\text{N}_2$  and exposed to air only during the PL measurements. As shown in Figure 4h, the PL intensities for both states are stable over up to 10 d, implying that the 2D/FeFET devices are potentially superior in data retention over contemporary FeFET devices constructed with thick semiconductor channels that typically show much data loss within similar period of time.<sup>[49]</sup>

What follows is a discussion on the fundamental advantage of the 2D/FeFET memories over conventional Si-based FeFETs. This can be analyzed in terms of the depolarization field,  $E_D$ , built up in the opposing direction to the FE polarization, as depicted in Figure 5a. Unless compensating charges of opposite signs are accumulated in the vicinity of the FE to fully screen the polarization charges, such as in the case of metal- $\text{FE}$ -metal capacitors (Figure 5b),  $E_D$  would exist which tends to suppress the spontaneous polarization.<sup>[26,27]</sup> Generally, in the FeFET structure, one side of the FE film is in contact with a semiconductor channel as opposed to a metal, and hence the  $E_D$  cannot be completely eliminated, thus limiting the memory retention. In this case,  $E_D$  is given by  $E_D = P/[\epsilon_0\epsilon_f((C_S/C_f) + 1)]$  in absence of external fields, where  $P$ ,  $\epsilon_f$ , and  $C_f$  represent the polarization, the dielectric constant, and the capacitance of the FE, respectively, and  $C_S$  is the capacitance of the semiconductor part. This  $E_D$  is equal to  $E_{D0}/((C_S/C_f) + 1)$ , while  $E_{D0} = P/(\epsilon_0\epsilon_f)$  is the maximum  $E_D$  which occurs in the case of no charge screening (Figure 5a). Therefore,  $C_S$  is critically important to eliminate  $E_D$ .

The  $E_D$  values were calculated for 2D/FeFETs incorporating  $\text{WSe}_2$  or  $\text{MoS}_2$  channels as a function of the number of layers in comparison to Si-channel FeFET devices.<sup>[50]</sup> For the Si-based devices, the Si thickness was conservatively set as 20 nm, the typical thickness of Si channel in FETs.<sup>[51]</sup> More realistic FeFET devices including buffer layers such as  $\text{SiO}_x$  and  $\text{HfO}_2$  films

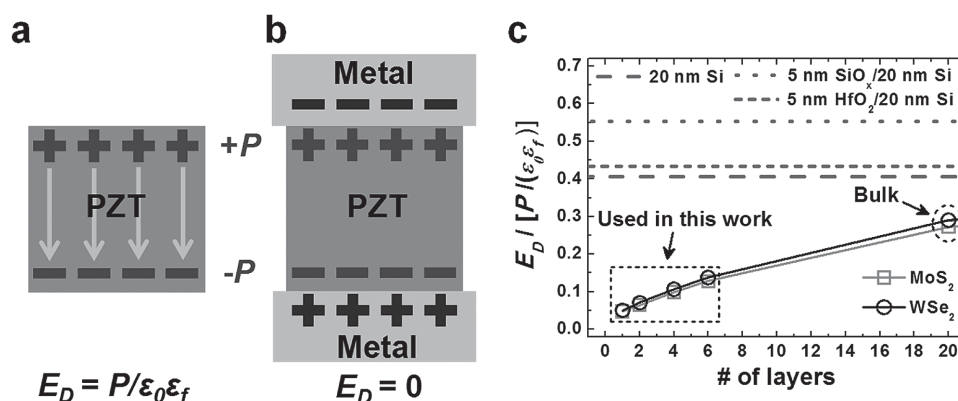


**Figure 5.** Depolarization field for various ferroelectric memory structures. a) If an isolated PZT thin film is polarized,  $E_D$  is formed in the opposite direction to that of the net  $P$ . b) When a polarized PZT is sandwiched by metal electrodes, charges of the opposite sign to the polarization charges are accumulated near the interface in the metal plates, nullifying  $E_D$  completely. c)  $E_D$  created in the PZT film in contact with the 2D TMD channel was calculated with various channel thickness.  $E_D$  is normalized to the maximum given by the situation illustrated in (a), which is equal to  $\approx 388.8 \text{ MV m}^{-1}$  for PZT. The normalized  $E_D$  computed for FeFET devices composed of 20 nm thick Si channels with or without 5 nm thick  $\text{SiO}_x$  or  $\text{HfO}_2$  buffer layers are also shown for comparison. Theoretical dielectric constants of 2D materials of various number of layers were obtained from Ref. [50]. The dielectric constant, film thickness and  $P$  of the PZT film used in this work, 200, 500 nm, and  $60 \mu\text{C cm}^{-2}$ , respectively, were employed for the calculations while the dielectric constants of Si,  $\text{SiO}_x$ , and  $\text{HfO}_x$  were 11.68, 3.9, and 25, respectively.

were also considered.<sup>[18]</sup> As summarized in Figure 5c, the calculated  $E_D$  values of 2D/FeFET structures are much lower than those of Si-based devices, suggesting that the memory retention of the FeFET devices with 2D TMD channels can be superior to those of Si-based counterparts.

To summarize, we have demonstrated NVM devices by interfacing 2D TMD channels with FE thin films. Adopting TMD layers as semiconducting channels can be used to circumvent major challenges faced in developing FeFETs, i.e., interface instability and depolarization-induced memory loss. Our prototype 2D/FeFET devices exhibit low switching voltages (<2.5 V), high on-off ratios ( $>10^4$ ), and superior data retention ( $>10$  d) comparable to those of conventional thin-film FeFETs. Also, considering the high-speed switching performance, the solid state 2D/FeFETs would be a promising candidate for ultrathin and flexible high-speed memory applications. The device performance may be further improved by optimizing the selection of the 2D TMDs and device structures, as well as by introducing FE materials (such as BiFeO<sub>3</sub>) with stronger polarization.<sup>[52,53]</sup> In parallel with the electronic memory function, a nonvolatile modulation of the light emission spectrum was also demonstrated using monolayer TMDs. Our results show that unprecedented functionalities could be developed from synergy across the interface between highly dissimilar materials.

## Experimental Section

**PZT Thin-Film Growth:** PZT (500 nm) and SRO (50 nm) thin films were grown epitaxially on (001) single-crystal STO substrates by PLD utilizing a KrF laser ( $\lambda \approx 248$  nm) under substrate temperature of 630 and 750 °C, respectively. During the deposition, a small amount of O<sub>2</sub> gas was introduced into the chamber with the total pressure fixed at  $\approx 100$  mTorr. Following deposition of the PZT/SRO structures, the films were cooled back down to room temperature at an O<sub>2</sub> pressure of 500 Torr with a cooling rate of 5 °C min<sup>-1</sup>.

**2D TMD Layer Preparation:** Most of WSe<sub>2</sub> and MoS<sub>2</sub> flakes were mechanically exfoliated onto the PZT thin films from single crystals of WSe<sub>2</sub> (grown by vapor transport technique) and MoS<sub>2</sub> (purchased from SCI). Some TMD flakes were exfoliated on SiO<sub>2</sub>/Si substrates first and wet-transferred to the PZT surface using poly(methyl methacrylate) (PMMA). The process of WSe<sub>2</sub> single crystal growth is described in detail in the Supplementary Note 1.

**Device Fabrication and Electrical Transport Measurements:** Standard electron beam lithography was employed for patterning the electrodes. XeF<sub>2</sub> etching was used to pattern the exfoliated flakes into rectangular shapes. Pt/Au (for both few-layer WSe<sub>2</sub> and MoS<sub>2</sub>) or Ti/Au (only for monolayer MoS<sub>2</sub>) metal contacts with 10 nm/70 nm thicknesses were formed by e-beam evaporation and subsequent lift-off process. Back-gated FET characterization was performed on a conventional probe station using two Keithley 617 programmable electrometers to monitor both the drain and source-bottom gate currents simultaneously. Channel current-voltage characteristic curves were also measured separately via a NI BNC-2090 A/D board and a current amplifier.

**Micro-PL and Raman Measurements:** PL and Raman measurements were conducted using a 100× objective lens on a Renishaw micro-Raman/PL system equipped with an excitation laser ( $\lambda \approx 488$  nm). The laser power was set properly in the range from 0.1 to 1  $\mu$ W on the spot with an area of  $\approx 1 \mu\text{m}^2$ , to avoid any damage on the 2D materials.

## Supporting Information

Supporting Information is available from the Wiley Online Library or from the author.

## Acknowledgements

This work was supported by a NSF CAREER Award under the Grant No. DMR-1055938. The 2D materials preparation and processing were partially supported by a NSF grant under the Grant No. DMR-1306601. Y.L. is supported by the NSF-TANMS Center and J.D.C. is supported by a SRC FAME program. C.K. and J.W. conceived the research and designed the experiments. C.K. carried out all the optical and electrical measurements and data analysis. Y.L., J.D.C. and R.R. grew and characterized the PZT films. C.K., Y.C., J.S., D.F., S.L., and H.S.C. prepared the 2D flakes and fabricated the devices collaboratively. A.S. and S.T. synthesized the WSe<sub>2</sub> single crystals. The project was supervised by J.W. All the authors discussed results and contributed to writing the manuscript. The authors declare no competing financial interests. The authors thank Dr. Eunpa Kim, Prof. Kai Liu, and Dr. Deyang Chen for useful discussions and appreciate Taegyung Park's assistance in 2D material preparation.

Received: September 28, 2015

Revised: December 16, 2015

Published online: February 19, 2016

- [1] K. Roy, M. Padmanabhan, S. Goswami, T. P. Sai, G. Ramalingam, S. Raghavan, A. Ghosh, *Nat. Nanotechnol.* **2013**, *8*, 826.
- [2] Y. Gong, J. Lin, X. Wang, G. Shi, S. Lei, Z. Lin, X. Zou, G. Ye, R. Vajtai, B. I. Yakobson, H. Terrones, M. Terrones, Beng K. Tay, J. Lou, S. T. Pantelides, Z. Liu, W. Zhou, P. M. Ajayan, *Nat. Mater.* **2014**, *13*, 1135.
- [3] C.-H. Lee, G.-H. Lee, A. M. van der Zande, W. Chen, Y. Li, M. Han, X. Cui, G. Arefe, C. Nuckolls, T. F. Heinz, J. Guo, J. Hone, P. Kim, *Nat. Nanotechnol.* **2014**, *9*, 676.
- [4] S. Tongay, W. Fan, J. Kang, J. Park, U. Koldemir, J. Suh, D. S. Narang, K. Liu, J. Ji, J. Li, R. Sinclair, J. Wu, *Nano Lett.* **2014**, *14*, 3185.
- [5] X. Cui, G.-H. Lee, Y. D. Kim, G. Arefe, P. Y. Huang, C.-H. Lee, D. A. Chenet, X. Zhang, L. Wang, F. Ye, F. Pizzocchero, B. S. Jessen, K. Watanabe, T. Taniguchi, D. A. Muller, T. Low, P. Kim, J. Hone, *Nat. Nanotechnol.* **2015**, *10*, 534.
- [6] S. H. H. Shokouh, A. Pezeshki, S. R. Ali Raza, H. S. Lee, S.-W. Min, P. J. Jeon, J. M. Shin, S. Im, *Adv. Mater.* **2015**, *27*, 150.
- [7] C. Baeumer, D. Saldana-Greco, J. M. P. Martinez, A. M. Rappe, M. Shim, L. W. Martin, *Nat. Commun.* **2015**, *6*, 6136.
- [8] K. F. Mak, C. Lee, J. Hone, J. Shan, T. F. Heinz, *Phys. Rev. Lett.* **2010**, *105*, 136805.
- [9] H. Zeng, J. Dai, W. Yao, D. Xiao, X. Cui, *Nat. Nanotechnol.* **2012**, *7*, 490.
- [10] A. Chernikov, T. C. Berkelbach, H. M. Hill, A. Rigosi, Y. Li, O. B. Aslan, D. R. Reichman, M. S. Hybertsen, T. F. Heinz, *Phys. Rev. Lett.* **2014**, *113*, 076802.
- [11] W. Wu, L. Wang, Y. Li, F. Zhang, L. Lin, S. Niu, D. Chenet, X. Zhang, Y. Hao, T. F. Heinz, J. Hone, Z. L. Wang, *Nature* **2014**, *514*, 470.
- [12] B. Radisavljevic, M. B. Whitwick, A. Kis, *ACS Nano* **2011**, *5*, 9934.
- [13] B. Radisavljevic, A. Radenovic, J. Brivio, V. Giacometti, A. Kis, *Nat. Nanotechnol.* **2011**, *6*, 147.
- [14] Z. Yin, H. Li, H. Li, L. Jiang, Y. Shi, Y. Sun, G. Lu, Q. Zhang, X. Chen, H. Zhang, *ACS Nano* **2012**, *6*, 74.
- [15] G.-H. Lee, Y.-J. Yu, X. Cui, N. Petrone, C.-H. Lee, M. S. Choi, D.-Y. Lee, C. Lee, W. J. Yoo, K. Watanabe, T. Taniguchi, C. Nuckolls, P. Kim, J. Hone, *ACS Nano* **2013**, *7*, 7931.
- [16] M. Sup Choi, G.-H. Lee, Y.-J. Yu, D.-Y. Lee, S. Hwan Lee, P. Kim, J. Hone, W. Jong Yoo, *Nat. Commun.* **2013**, *4*, 1624.
- [17] S. Mathews, R. Ramesh, T. Venkatesan, J. Benedetto, *Science* **1997**, *276*, 238.
- [18] H. Ishiwara, *J. Semicond. Technol. Sci.* **2001**, *1*, 1.
- [19] Y. Y. Sung-Min, H. Ishiwara, *IEEE Trans. Electron Devices* **2001**, *48*, 2002.

- [20] C.-B. Eom, S. Trolrier-McKinstry, *MRS Bull.* **2012**, *37*, 1007.
- [21] R. Bruchhaus, D. Pitzer, M. Schreiter, W. Wersing, *J. Electroceram.* **1999**, *3*, 151.
- [22] S. S. Gevorgian, E. L. Kollberg, *IEEE Trans. Microwave Theory Tech.* **2001**, *49*, 2117.
- [23] R. Ramesh, S. Aggarwal, O. Auciello, *Mater. Sci. Eng. R* **2001**, *32*, 191.
- [24] H. Kohlstedt, Y. Mustafa, A. Gerber, A. Petraru, M. Fitsilis, R. Meyer, U. Böttger, R. Waser, *Microelectron. Eng.* **2005**, *80*, 296.
- [25] N. Setter, D. Damjanovic, L. Eng, G. Fox, S. Gevorgian, S. Hong, A. Kingon, H. Kohlstedt, N. Y. Park, G. B. Stephenson, I. Stolitchnov, A. K. TagansteV, D. V. Taylor, T. Yamada, S. Streiffner, *J. Appl. Phys.* **2006**, *100*, 051606.
- [26] C. T. Black, C. Farrell, T. J. Licata, *Appl. Phys. Lett.* **1997**, *71*, 2041.
- [27] T. P. Ma, J.-P. Han, *IEEE Electron Device Lett.* **2002**, *23*, 386.
- [28] H. S. Lee, S.-W. Min, M. K. Park, Y. T. Lee, P. J. Jeon, J. H. Kim, S. Ryu, S. Im, *Small* **2012**, *8*, 3111.
- [29] Y. T. Lee, H. Kwon, J. S. Kim, H.-H. Kim, Y. J. Lee, J. A. Lim, Y.-W. Song, Y. Yi, W.-K. Choi, D. K. Hwang, S. Im, *ACS Nano* **2015**, *9*, 10394.
- [30] X. Wang, P. Wang, J. Wang, W. Hu, X. Zhou, N. Guo, H. Huang, S. Sun, H. Shen, T. Lin, M. Tang, L. Liao, A. Jiang, J. Sun, X. Meng, X. Chen, W. Lu, J. Chu, *Adv. Mater.* **2015**, *27*, 6538.
- [31] S. Horiuchi, Y. Tokura, *Nat. Mater.* **2008**, *7*, 357.
- [32] A. Lipatov, P. Sharma, A. Gruverman, A. Sinitskii, *ACS Nano* **2015**, *9*, 8089.
- [33] X.-W. Zhang, D. Xie, J.-L. Xu, Y.-L. Sun, X. Li, C. Zhang, R.-X. Dai, Y.-F. Zhao, X.-M. Li, H.-W. Zhu, *IEEE Electron Device Lett.* **2015**, *1*.
- [34] S. Bertolazzi, D. Krasnozhan, A. Kis, *ACS Nano* **2013**, *7*, 3246.
- [35] K. Kang, S. Xie, L. Huang, Y. Han, P. Y. Huang, K. F. Mak, C.-J. Kim, D. Muller, J. Park, *Nature* **2015**, *520*, 656.
- [36] A. E. Nguyen, P. Sharma, T. Scott, E. Preciado, V. Klee, D. Sun, I. H. Lu, D. Barroso, S. Kim, V. Y. Shur, A. R. Akhmatkhanov, A. Gruverman, L. Bartels, P. A. Dowben, *Nano Lett.* **2015**.
- [37] K. F. Mak, K. He, C. Lee, G. H. Lee, J. Hone, T. F. Heinz, J. Shan, *Nat. Mater.* **2013**, *12*, 207.
- [38] W. Zhao, Z. Ghorannevis, L. Chu, M. Toh, C. Kloc, P.-H. Tan, G. Eda, *ACS Nano* **2013**, *7*, 791.
- [39] W. Zhao, R. M. Ribeiro, M. Toh, A. Carvalho, C. Kloc, A. H. Castro Neto, G. Eda, *Nano Lett.* **2013**, *13*, 5627.
- [40] W. Zhou, Z. Yin, Y. Du, X. Huang, Z. Zeng, Z. Fan, H. Liu, J. Wang, H. Zhang, *Small* **2013**, *9*, 140.
- [41] W. J. Merz, *Phys. Rev.* **1954**, *95*, 690.
- [42] C. F. Pulvari, W. Kuebler, *J. Appl. Phys.* **1958**, *29*, 1315.
- [43] O. Lohse, M. Grossmann, U. Boettger, D. Bolten, R. Waser, *J. Appl. Phys.* **2001**, *89*, 2332.
- [44] C. Zhou, X. Wang, S. Raju, Z. Lin, D. Villaroman, B. Huang, H. L.-W. Chan, M. Chan, Y. Chai, *Nanoscale* **2015**, *7*, 8695.
- [45] D. J. Late, B. Liu, H. S. S. R. Matte, V. P. Dravid, C. N. R. Rao, *ACS Nano* **2012**, *6*, 5635.
- [46] G. Arlt, *Ferroelectrics* **1987**, *76*, 451.
- [47] S. Tongay, J. Zhou, C. Ataca, J. Liu, J. S. Kang, T. S. Matthews, L. You, J. Li, J. C. Grossman, J. Wu, *Nano Lett.* **2013**, *13*, 2831.
- [48] S. Mouri, Y. Miyauchi, K. Matsuda, *Nano Lett.* **2013**, *13*, 5944.
- [49] H. Ishiura, *Integr. Ferroelectr.* **2006**, *79*, 3.
- [50] A. Kumar, P. K. Ahluwalia, *Physica B* **2012**, *407*, 4627.
- [51] H. S. P. Wong, *IBM J. Res. Dev.* **2002**, *46*, 133.
- [52] Y. Kwi Young, R. Dan, K. Takeshi, N. Minoru, O. Masanori, *Jpn. J. Appl. Phys.* **2004**, *43*, L647.
- [53] C.-M. Lin, W.-c. Shih, I. Y.-k. Chang, P.-C. Juan, J. Y.-m. Lee, *Appl. Phys. Lett.* **2009**, *94*, 142905.

# ADVANCED MATERIALS

## Supporting Information

for *Adv. Mater.*, DOI: 10.1002/adma.201504779

Ferroelectrically Gated Atomically Thin Transition-Metal  
Dichalcogenides as Nonvolatile Memory

*Changhyun Ko, Yeonbae Lee, Yabin Chen, Joonki Suh, Deyi Fu, Aslihan Suslu, Sangwook Lee, James David Clarkson, Hwan Sung Choe, Sefaatin Tongay, Ramamoorthy Ramesh, and Junqiao Wu\**

Copyright WILEY-VCH Verlag GmbH & Co. KGaA, 69469 Weinheim, Germany, 2013.

## Supporting Information

### **Ferroelectrically gated atomically thin transition metal dichalcogenides as non-volatile memory**

*Changhyun Ko, Yeonbae Lee, Yabin Chen, Joonki Suh, Deyi Fu, Aslihan Suslu, Sangwook Lee, James David Clarkson, Hwan Sung Choe, Sefaatin Tongay, Ramamoorthy Ramesh, and Junqiao Wu\**

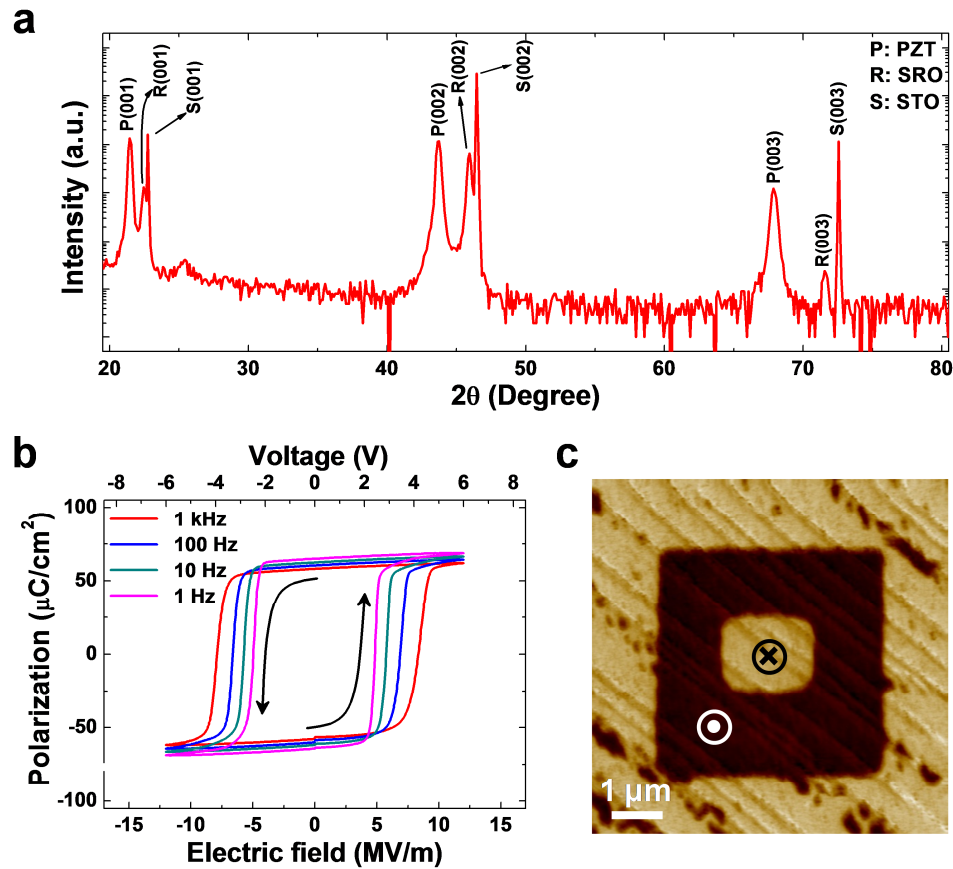


**Figure S1. Structural and piezo/ferroelectric characterizations of PZT thin films.** (a)  $2\theta$ - $\theta$  X-ray diffraction (XRD) spectrum of a PZT/SRO bilayer grown on a (001) STO single crystal substrate in the use of the Panalytical X'Pert Pro diffractometer (Philips Inc.) equipped with  $\text{Cu K}\alpha_1$  radiation source. The XRD identifies only (001), (002), and (003) peaks of the PZT and SRO films parallel to the (001) plane of the STO substrate confirming the epitaxial quality of PZT and SRO layers. (b) Polarization and electric field ( $P$  vs.  $E$ ) loops of a PZT film at varying frequency, ranging from 0.1 Hz to 1 kHz. The  $P$  vs.  $E$  curves were measured on PZT/SRO structures sandwiched between the STO substrates and Pt/Au metal contacts (10 nm/70 nm thicknesses) of  $40 \mu\text{m} \times 40 \mu\text{m}$  size on Radiant ferroelectric analyzer. The remnant polarization value was

estimated to be  $\sim 60 \mu\text{C}/\text{cm}^2$ . (c) Out-of-plane piezoresponse force microscopy (PFM) images to visualize electric-field-dependent domain structure after applying tip biases of  $-6.0 \text{ V}$  and  $+6.0 \text{ V}$  scanning  $3 \mu\text{m} \times 3 \mu\text{m}$  and  $1 \mu\text{m} \times 1 \mu\text{m}$  areas respectively. The label on the graph indicates the polarization direction with dark region pointing up and bright region down. Both the  $P$  vs.  $E$  results and PFM images strongly support piezo/ferroelectricity of the PZT films and bulk-like  $180^\circ$  polarization switching mechanism.

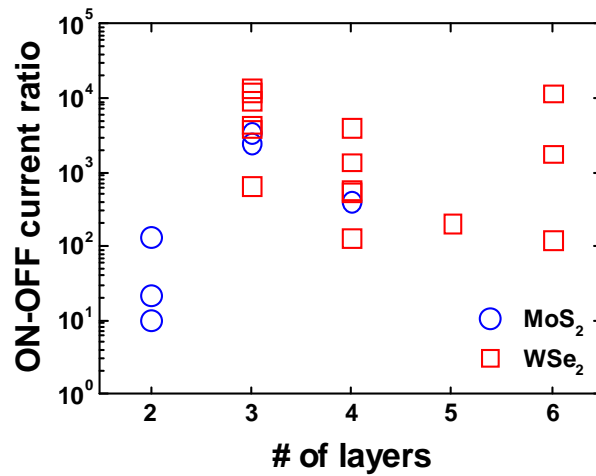


**Figure S2. Channel current ON-OFF ratio of FeFET devices based on 2D channels of various thicknesses.** In the range from three to six layers, significant thickness-dependence of on-off ratio was not observed in both p- and n-channels. However, in the case of bilayers, the memory performance is worse to the thicker channels probably since the off-state current was much lower than the equipment limit (0.01 pA) and it is more difficult to fabricate good contact as flakes thickness get thinner. The single-layer MoS<sub>2</sub> device only showed FET characteristics with no memory function maybe due to the same reasons (not shown here). The fluctuation in the ON-OFF current ratio is likely due to multiple reasons including the contact resistance, structural and chemical inhomogeneity, and surface contamination and nanoscale deformation of the 2D channels. Endeavors need to be made to improve synthesis and fabrication protocols to minimize these extrinsic effects for scrutinizing the thickness-dependent intrinsic electrical properties of 2D materials on PZT films, as well as for thinning the channels toward monolayers.

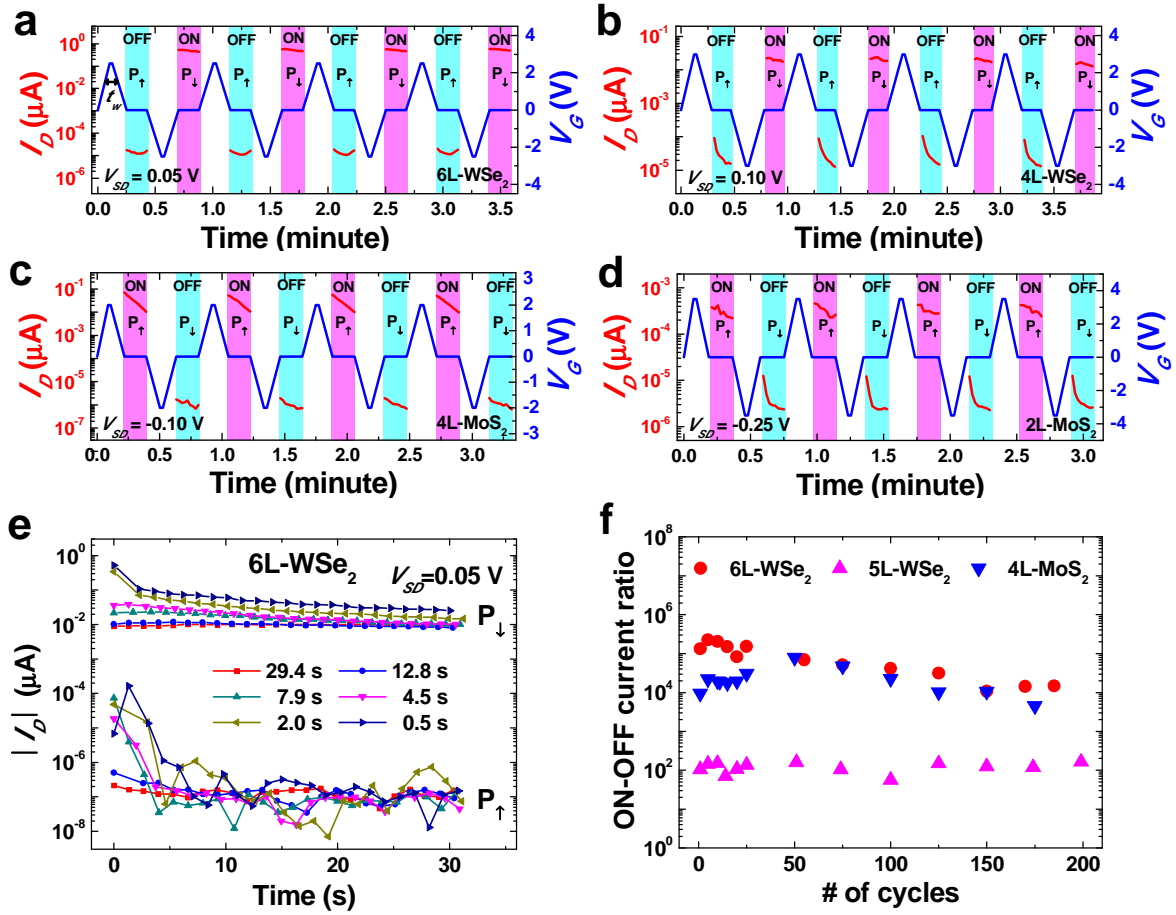


**Figure S3. Switching operations of ferroelectric field-effect transistor devices.** On the FeFET devices based on p-type (a) 6L-WSe<sub>2</sub> and (b) 4L-WSe<sub>2</sub> and n-type (c) 4L-MoS<sub>2</sub> and (d) 2L-MoS<sub>2</sub>,  $I_D$  (red) of ON and OFF states was measured after the FE poling with  $V_G$  (blue) during multiple switching cycles. The gate pulse peak voltage ( $V_P$ ) and the full width at half maximum (FWHM) time width ( $t_w$ ) were fixed at (a)  $\pm 2.5$  V and  $\sim 7.9$  s, (b)  $\pm 3.0$  V and  $\sim 9.4$  s, (c)  $\pm 2.0$  V and  $\sim 6.5$  s, and (d)  $\pm 3.5$  V and  $\sim 6.1$  s keeping the source-drain voltage ( $V_{SD}$ ) as (a) 0.05 V, (b) 0.1 V, (c) -0.1 V, and (d) -0.25 V, respectively, for each during multiple switching cycle. (e) Using the 6L-WSe<sub>2</sub> FeFET device, channel current relaxation was observed immediately after pulsed-gating

with various  $t_w$  at ON (down-polarized,  $P_{\downarrow}$ ) and OFF (up-polarized,  $P_{\uparrow}$ ) states, maintaining the  $V_{SD}$  as 0.05 V. (f) Data endurance test by monitoring ON-OFF channel current ratio under repeated switching cycles on the chosen FeFET devices, setting  $V_P$  as  $\pm 2.0$  V,  $\pm 2.5$  V, and  $\pm 3.0$  V,  $V_{SD}$  as -0.1 V, 0.05 V, and 0.1 V, and  $t_w$  as  $\sim 6.5$  s,  $\sim 7.9$  s, and  $\sim 8.6$  s for the 4L-MoS<sub>2</sub>, 6L-WSe<sub>2</sub>, and 5L-WSe<sub>2</sub> channels, respectively.  $I_D$  values used to calculate ON-OFF ratio are the average current over 5 s after 5 s post-switching relaxation.

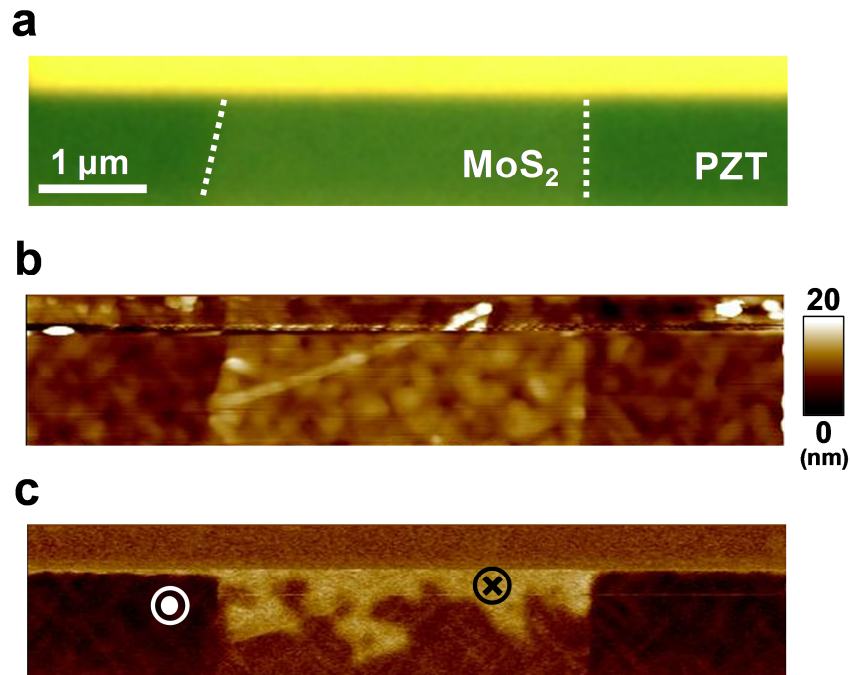


**Figure S4. Spreading of ferroelectric domain switching under 2D channel by piezoresponse force microscopy.** (a) Optical microscopy image of the 3L-MoS<sub>2</sub> flake on the PZT with a metal electrode for top gating using a metal-coated atomic force microscopy (AFM) tip. (b) and (c) are the topography map of contact AFM and the out-of-plane piezoresponse force microscopy (PFM) image taken from the identical flake simultaneously after applying a tip bias of +5 V through the metal electrode. The as-grown PZT film was mostly up-polarized (dark). On the uncovered region of PZT, the domains beneath the metal electrode can be switched to down-polarized state (bright). However, in the case of the PZT coated with the 2D semiconductor, the domain switching was observed to spread out from the electrodes almost up to 1 μm under the 2D channel indicating that 2D layer can function as a conducting pad to some extent.

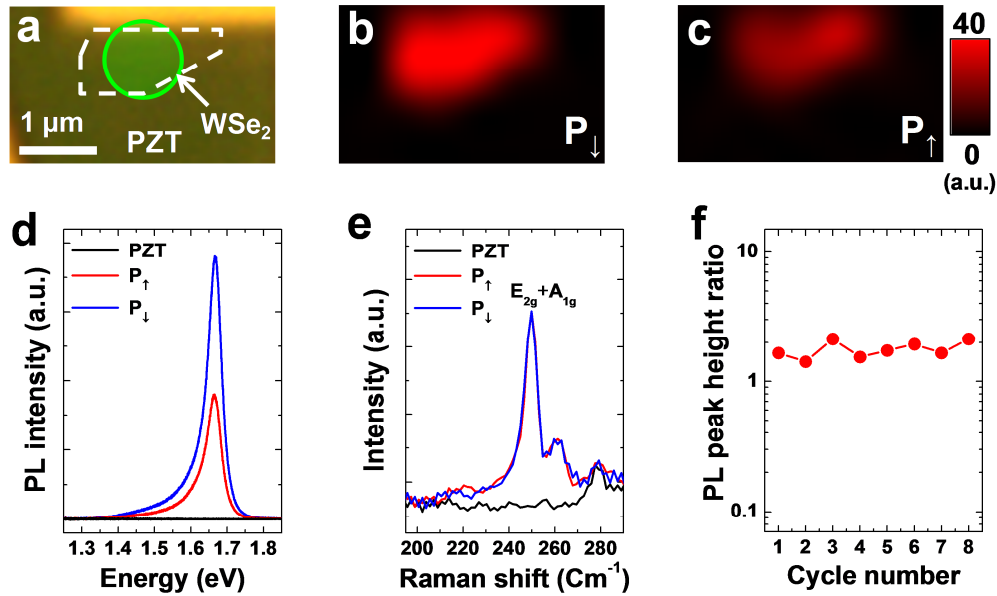


**Figure S5. Non-volatile photoluminescence modulation of WSe<sub>2</sub> monolayer driven by the ferroelectric gating.** (a) Optical microscopy image taken from a 1L-WSe<sub>2</sub> flake on PZT. (b) and (c) are the maps of integrated PL intensity in the down- ( $P_{\downarrow}$ ) and up-polarized states ( $P_{\uparrow}$ ), respectively. (d) Photoluminescence (PL) and (e) Raman spectra measured from the WS<sub>2</sub> monolayer at both polarization states from the circle indicated in (a). PL and Raman spectra obtained from the bare PZT surface are also shown as background references. (f) PL peak height ratios of two polarization states was monitored under successive FE poling cycles showing that the PL tuning of 1L-WSe<sub>2</sub> is also reversible under FE gating like the case of 1L-MoS<sub>2</sub>.

**Supplementary Note 1.**

The single crystal growth of WSe<sub>2</sub> was achieved by vapor transport technique employing iodine as a transport agent through the following two step process.

(1) WSe<sub>2</sub> powder preparation. Polycrystalline WSe<sub>2</sub> powders were synthesized at 1065 °C for three days in a single zone furnace from tungsten and selenium 325-mesh powders of high purity (99.995%) with a molar ratio of 1:2.01 in evacuated quartz tubes. Then, materials were cooled down to room temperature controllably at the rate of 500 °C/hour.

(2) Single crystal WSe<sub>2</sub> growth. 2.5 g of the WSe<sub>2</sub> charges and I<sub>2</sub> granule (3 mg/cc) were introduced into quartz tubes (length = 22 cm). The quartz tube was evacuated to 2x10<sup>-6</sup> Torr, sealed and then, placed in a three-zone furnace coaxially. The three zones of furnace were heated to 1030 °C, 1000 °C and 940 °C, respectively. Powders were located in the hot zone ( $T_{precursor} = 1030$  °C) and synthesized crystals were collected in the cold zone ( $T_{growth} = 940$ °C). The total duration time of the growth was 3 weeks and eventually cooled down to room temperature gradually at the rate of 500 °C/hour.